ACS Photonics

Article

pubs.acs.org/journal/apchd5

Efficient Time-Dependent Monte Carlo Simulations of Stimulated Raman Scattering in a Turbid Medium

Brett H. Hokr,*[,†] Vladislav V. Yakovlev,[†] and Marlan O. Scully[†,‡,§]

[†]Texas A&M University, College Station, Texas, United States

[‡]Princeton University, Princeton, New Jersey, United States

[§]Baylor University, Baylor, Texas, United States

ABSTRACT: Monte Carlo methods have become the gold standard for investigating the properties of light transport in turbid media due to their simple conceptual picture and quantitative agreement with experiment. However, these approaches are limited to the study of linear effects. In this work, a model capable of efficiently and accurately simulating stimulated Raman scattering in a turbid environment is presented for the first time. The method is validated using both analytical calculations and experimental data. These results will allow for a deeper understanding of nonlinear light propagation in a turbid medium and will be indispensable in understanding the processes involved in random Raman lasing.

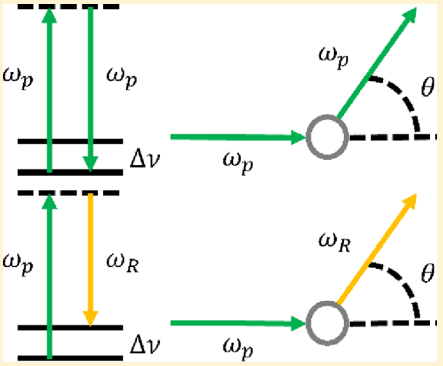

KEYWORDS: *Monte Carlo, stimulated Raman scattering, turbid media, random Raman lasing*

The propagation of light in the presence of scattering is a long-standing problem of fundamental importance. Everything from light-based biomedical imaging techniques to Earth-based telescopes are intimately effected by the scattering of light. The multiple elastic scattering which takes place in optically thick turbid media is mathematically intractable. From the viewpoint of Maxwell's equations, it requires knowledge of the location and shape of each individual scatterer. Ultimately, this would involve solving Maxwell's equations with tremendously complicated boundary conditions, making the problem virtually impossible. In contrast, Monte Carlo simulations describe light as discrete particles that scatter in random directions at random intervals. These discrete particles are referred to as photon packets to distinguish them from the physical quantum of light and indicate that a single photon packet can represent many more than a single physical photon. Monte Carlo simulations allow very complex dynamics to be simulated with only the knowledge of macroscopic physical properties of the medium. This allows anisotropic elastic scattering to be described using only two bulk material properties, the scattering coefficient and the average value of the scattering angle.[1−4] Historically, the major limitation in the application of Monte Carlo simulations has been their computationally intensive nature. Advances in computing power over the years, and more recently, the advances in graphics processing unit (GPU) computing, have made this largely a concern of the past.[5]

In addition to elastic scattering, Monte Carlo simulations have been made to handle the effects of absorption in much the same way. However, to reduce the variation from run to run, the concept of partial absorption is commonly used.[4,6] This allows the photon packet to be partially absorbed by defining a photon weight that is reduced as the photon packet propagates through the medium. Ultimately, when the photon packet's weight is reduced below a threshold value, a Russian roulette process is used to eliminate the photon packets in a way that conserves energy.[4]

Furthermore, Monte Carlo simulations have been extended to investigate other linear effects such as fluorescence[7−10] and spontaneous Raman scattering.[11−14] Various methods have been used to accomplish this, but the ones most in line with our present approach define an appropriate probability law (Beer's law in the case of linear effects), which describes the probability of a photon packet to undergo a certain process in a given step.

Traditionally, it is thought that the diffusion of light in a turbid media renders nonlinear effects unimportant. The recent discovery of random Raman lasing shows that this is not the case when intense pulses of light are used.[15,16] Other notable advances, involving wavefront optimization hint at the possibility of being able to focus light to a smaller region inside a turbid environment, further elucidate the need for a better understanding of nonlinear optics in the presence of scattering.[17,18] In addition to random Raman lasing, nonlinear Raman effects offer the possibility for noninvasive label-free biomedical sensing and imaging deep in tissue.[19−24]

To date, the only nonlinear effect to be considered by Monte Carlo techniques is multiphoton fluorescence.[25−27] These simulations rely on the computation of a linear response

Received: September 25, 2014
Published: November 25, 2014

   dx.doi.org/10.1021/ph5003522 | *ACS Photonics* 2014, 1, 1322−1329

function for the medium. This is computed by propagating a point source of photons, considering only absorption and elastic scattering, through the medium and keeping track of the photon density throughout the medium. The linear response function is then convolved with the pulse to be considered, and the effects of fluorescence are computed from the intensity distribution. This approach works well so long as the nonlinear effect remains weak and temporal dynamics can be ignored, as is often the case with multiphoton fluorescence. However, stimulated Raman scattering (SRS) is an instantaneous effect making transient dynamics important. Additionally, due to the presence of exponential gain SRS can saturate the pump pulse, making the assumption that the nonlinear effect does not effect the distributions of photons in the medium a poor one. Thus, in order to accurately describe the effects of SRS a new approach is required.

In this paper, a nonlinear Monte Carlo (NLMC) model for SRS is presented. The nonlinear effects are treated by deriving probability laws for a pump photon packet to be converted to a Stokes or anti-Stokes photon packet, which depend on the local density of photon packets. By treating the problem in this fashion, secondary effects such as pump depletion are automatically taken into account. This process is quite general and allows for generalization to other nonlinear effects. The model is then validated using both analytical and experimental results. In addition, the derived probability law is related back to physical parameters through comparison with one-dimensional propagation equations.

RESULTS

Model. The nonlinear Monte Carlo method presented here is based on a standard Monte Carlo multilayer (MCML) method.[4] For the sake of clarity and completeness, we will summarize the parts of the traditional MCML model that were used here.

To simulate nonlinear effects, such as SRS, knowledge is required of each photon packet's position at a given time. To include time resolution into the simulation, a global time step, Δt, is defined. Each photon packet is propagated independently during a single global time step. However, at the end of each time step, all the photon packets must be stopped and synchronized with each other. When the photon packets are synchronized, the photon densities required for treating SRS are computed. These photon densities are then used to calculate the nonlinear photon dynamics throughout the next global time step. This method allows for highly parallel computation and is subject only to the constraint that the photon packets cannot move far enough during a single global time step that they significantly alter the photon density. Samples with high elastic scattering are perfect from this standpoint, as multiple elastic scattering results in a speed of energy diffusion, which is slow compared to the speed of light, allowing a more course global time steps to be used without sacrificing accuracy. Once the combined weight of all the photons remaining in the simulation falls below a given threshold, for all simulations here this threshold is 0.001% of the initial weight, the simulation is terminated.

Initial Conditions. Pulses of light are initialized outside the turbid medium and formed by assigning (x, y, z) coordinates to N photon packets which satisfy the profile of the desired pulse. The simplest such pulse to consider would be a pulse that is incident on the sample that has both a Gaussian spatial and temporal profile. In this case, the initial distribution function of the pulse is given by

$$\rho(x, y, z) = \frac{1}{(2\pi)^{3/2}\sigma_r^2\sigma_\tau} \exp\left(-\frac{x^2 + y^2}{2\sigma_r^2} - \frac{(z/c - \delta\tau)^2}{2\sigma_\tau^2}\right) \tag{1}$$

where c is the speed of light in a vacuum, $\delta\tau$ is a delay that is assigned to keep the pulse out of the turbid medium at the start of the simulation, σ_r is the standard deviation in both the x and y directions, and σ_τ is the standard deviation in the t direction. The $1/e^2$ width of the beam relates to the standard deviation by $w = 4\sigma_r$ and the full-width at half-maximum pulse length is related by $\Delta\tau = 2(2\ln(2)\sigma_\tau)^{1/2}$. The front surface of the sample is always taken to be the $z = 0$ plane. To sample a Gaussian distribution with a uniform pseudorandom number generator, the Box-Mueller method was used.[28] This produces two independent normally distributed random numbers, χ_1 and χ_2, from two independent uniform random numbers, ξ and η,

$$R = \sqrt{2\sigma^2 \ln\left(\frac{1}{1 - \xi}\right)} \tag{2}$$

$$\theta = 2\pi\eta \tag{3}$$

$$\chi_1 = R\cos(\theta) \tag{4}$$

$$\chi_2 = R\sin(\theta) \tag{5}$$

In addition to Gaussian distributions, arbitrary distributions can be sampled by integrating and then inverting the following equation for χ:

$$\int_a^\chi \rho(x)\mathrm{d}x = \xi \tag{6}$$

Here, a represents the minimum value of the independent variable of the distribution, and ξ is a uniformly distributed random number between 0 and 1. In order to allow arbitrary distributions to be handled, eq 6 must be numerically solved. In our implementation, the numerical integration is accomplished using Simpson's method[29] and Brent's method for the numerical inversion.[30] This produced a stable and reliable method for generating arbitrary distributions.

In addition to prescribing the initial positions of the photon packets, the initial direction must also be specified. In the most simple case of a collimated beam normally incident on the sample, the direction vector would be identical for all photon packets and be given by $\mathbf{v} = \langle 0, 0, 1\rangle$. A focusing pulse can also be simulated by way of a coordinate transformation from collimated space to focusing space. To start, we initialize the photon packets as if there was no lens present giving each photon packet its collimation space location, $\mathbf{r} = \langle x, y, z\rangle$. Then the focusing space coordinates for that particle are given by

$$x' = \frac{xz}{\sqrt{x^2 + y^2}} \sin\left(2\frac{\sqrt{x^2 + y^2}}{d_0}\psi\right) \tag{7}$$

$$y' = \frac{yz}{\sqrt{x^2 + y^2}} \sin\left(2\frac{\sqrt{x^2 + y^2}}{d_0}\psi\right) \tag{8}$$

$$z' = z\cos\left(2\frac{\sqrt{x^2 + y^2}}{d_0}\psi\right) \tag{9}$$

dx.doi.org/10.1021/ph5003522 | ACS Photonics 2014, 1, 1322−1329

Here d_0 is the diameter of lens, and ψ is the angle that the focusing cone makes with the propagation axis, given in terms of the numerical aperture by $\psi = \sin^{-1}(\mathrm{NA})$. The direction vector of these focusing photons is $\mathbf{v}' = -\mathbf{r}'/|\mathbf{r}'|$. After the velocities are assigned, the depth of focus, z_f, can be assigned by a further translation, $z' \rightarrow z' + z_f$. It should be noted that wave effects like the diffraction limit are neglected by this approach. However, in the presence of scattering, this is not a major concern as the pulse will be sufficiently scattered prior to reaching a nonphysical, subdiffraction limited size.

The target sample is composed of different layers. Each layer is described by a set of parameters which determine the optical properties of that layer. These parameters are the index of refraction, n, the elastic scattering coefficient, μ_s, the anisotropy factor, g, the absorption coefficient, μ_a, the Raman scattering coefficient, μ_R, the SRS coefficient, μ_{SRS}. For the purpose of including reflection and refraction at the surface, the medium surrounding the sample is given an index of refraction, n_0, and is assumed to have no scattering or absorption.

Elastic Scattering. The distance a photon travels between scattering events is described by the exponential distribution

$$\rho(d) = \mu_s e^{-\mu_s d} \tag{10}$$

where μ_s is the elastic scattering coefficient. Using eq 6, the dimensionless distance a photon travels to its next elastic scattering event is given by

$$s = \mu_s d = -\ln(1 - \xi_1) = -\ln(\xi_1) \tag{11}$$

where the last step makes use of the symmetry of a uniform random number, ξ_1, around 0.5. Once s is assigned, the dimensionless length to the next boundary is calculated by

$$s_b = \frac{(z_b - z)\mu_s}{v_z} \tag{12}$$

Here, $z_b - z$ is the distance along the z-axis from the photon packet to the nearest boundary that the photon will hit, μ_s is the elastic scattering coefficient in the region the photon packet is currently in, and v_z is the z-component of the photon packet's direction vector. Next, to keep the photons synchronized, we must calculate the dimensionless length that the photon will travel in the current global time step

$$s_t = \frac{c(i\Delta t - t)\mu_s}{n} \tag{13}$$

Here, c is the speed of light in vacuum, n is the index of refraction of the current region, and i is the counter that keeps track of the number of global time steps which have elapsed. Thus, $i\Delta t - t$ is a measure of how much time is left before the next synchronization. It is useful to define the dimensionless distance the photon packet will travel before it elastically scatters, encounters a boundary, or must pause to be synchronized with the other photon packets to be Δs

If s_t is less than either s and s_b, then $\Delta s = s_t$, and the photon packet will move in a straight line until the next synchronization. It will then wait for all other photon packets to reach this point before continuing. The new positions of the photon packet are given by

$$\mathbf{r}' = \mathbf{r} + \frac{\Delta s}{\mu_s}\mathbf{v} \tag{14}$$

If s is less than either s_b and s_t, then $\Delta s = s$ and the photon packet will move in a straight line to its next scattering event, using eq 14, where it will get a new direction vector, $\mathbf{v}'$, given by[31]

$$v'_x = \frac{v_y \sin(\phi) - v_x v_z \cos(\phi)}{\sqrt{1 - v_z^2}}\sin(\theta) + v_x \cos(\theta) \tag{15}$$

$$v'_y = -\frac{v_x \sin(\phi) + v_y v_z \cos(\phi)}{\sqrt{1 - v_z^2}}\sin(\theta) + v_y \cos(\theta) \tag{16}$$

$$v'_z = \sqrt{1 - v_z^2}\cos(\phi)\sin(\theta) + v_z \cos(\theta) \tag{17}$$

In the case where $|v_z| = 1$, these equations reduce to

$$v'_x = \sin(\theta)\cos(\phi) \tag{18}$$

$$v'_y = \sin(\theta)\sin(\phi) \tag{19}$$

$$v'_z = v_z \cos(\theta) \tag{20}$$

The scattering angle, θ, is given by the Henyey-Greenstein distribution function,

$$\cos(\theta) = \frac{1}{2g}\left[1 + g^2 - \left(\frac{1 - g^2}{1 - g + 2g\xi_2}\right)^2\right] \tag{21}$$

Here, ξ_2 is a uniform random number between 0 and 1. In the case of isotropic scattering, the anisotropy factor, $g = \langle\cos(\theta)\rangle = 0$ the Henyey-Greenstein distribution reduces to $\cos(\theta) = 2\xi_2 - 1$. Scattering is assumed to be symmetric about the z-axis, thus, the azimuthal angle is simply

$$\phi = 2\pi\xi_3 \tag{22}$$

where ξ_3 is another uniform random number between 0 and 1.

If s_b is less than either s and s_t, then $\Delta s = s_b$, and the photon will move in a straight line to the nearest boundary, using eq 14, where it will undergo reflection or refraction in accordance to Fresnel's and Snell's laws. When a photon packet is incident on a boundary, either between two sample layers or between one layer and the background medium, Fresnel's law is applied to determine the probability of the photon packet reflecting off the boundary. If the index of refraction of the region that the photon is currently in, n_o, is larger than the index of refraction of region the photon is trying to transmit to, n_n, and the angle of incidence, α_i, is such that $\alpha_i > \sin^{-1}(n_n/n_o)$, then total internal reflection occurs and the photon is assigned a probability of reflecting of $R = 1$. When these conditions are not fulfilled, the probability that the photon packet reflects at the boundary is given by Fresnel's law,

$$R = \frac{1}{2}\left\{\frac{[n_o \cos(\alpha_t) - n_n \cos(\alpha_i)]^2}{[n_o \cos(\alpha_t) + n_n \cos(\alpha_i)]^2} + \frac{[n_o \cos(\alpha_i) - n_n \cos(\alpha_t)]^2}{[n_o \cos(\alpha_i) + n_n \cos(\alpha_t)]^2}\right\} \tag{23}$$

The transmission angle is determined by Snell's law

$$\alpha_t = \sin^{-1}\left[\frac{n_o}{n_n}\sin(\alpha_i)\right] \tag{24}$$

dx.doi.org/10.1021/ph5003522 | ACS Photonics 2014, 1, 1322−1329

The photon packet then transmits at the boundary with the refracted angle α_t, if $R > \xi_4$, where ξ_4 is a uniformly distributed random number between zero and unity, otherwise the photon packet is reflected with the new direction $\mathbf{v}' = \langle v_x, v_y, -v_z \rangle$.

Once one of these three outcomes have occurred, the dimensionless distance remaining until the photon elastically scattered is updated using $s = s - \Delta s$. When $s = 0$, eq 11 is used and a new dimensionless distance to the next elastic scattering event is assigned and the process is repeated until the simulation terminates.

Absorption. Absorption is treated using the Russian roulette method.[4,6] In this technique, each photon packet is assigned a weight, typically equal to unity to start. When a photon travels a distance of Δs, the photons new weight, w', is given by

$$w' = e^{-\mu_a(\Delta s/\mu_s)}w \tag{25}$$

Once the photons weight shrinks below a threshold value, w_t, the photon has a probability of p of being removed from the simulation. In our work, we set $w_t = 10^{-6}$ to minimize the error incurred from this simplifying approximation. If the photon survives, it is given a new weight of $w' = (1/p)w$ and continues to propagate in the simulation. This has been shown to be a viable method of accurately simulating the effects of absorption while decreasing the variance of the simulations.[6]

Spontaneous Raman Scattering. Spontaneous Raman scattering is a linear process just like elastic scattering and absorption, thus it can be treated in a similar manner. The probability that a pump photon undergoes spontaneous Raman scattering over a dimensionless distance Δs is given by

$$P_R = 1 - e^{-\beta_R(\Delta s/\mu_s)} \tag{26}$$

If a uniform random number $\xi_5 < P_R$ then the photon is converted into a Raman photon. Raman scattering is assumed to be isotropic, thus the new direction vector is given by eqs 18−20 with the scattering angles given by

$$\cos(\theta) = 2\xi_2 - 1 \tag{27}$$

$$\phi = 2\pi\xi_3 \tag{28}$$

Multiple orders of Raman scattering could be treated; however, in our simulations, we neglect these higher order Raman processes.

Stimulated Raman Scattering. To treat SRS in the simulation, we must have knowledge of the distribution of Raman scattered photons. This distribution is computed by assigning a grid of voxels to the computational domain then summing up the weight of each Raman photon located in each bin. This is computed only at the end of each global time step; thus, the global time step itself must be chosen small enough such that the photon distribution does not undergo large changes during the course of a single time step. The probability that a pump photon undergoes a SRS process is given by

$$P_{SRS} = 1 - e^{-\beta_{SRS}\rho_R(\Delta s/\mu_s)} \tag{29}$$

Here, ρ_R is the local Raman photon packet density. This is computed by summing the total weight of Raman photons in the same voxel and then dividing by the volume of the voxel. The new direction is taken to be the weighted average of the direction vectors of Raman photons in the same voxel.

Validation. To ensure the basic elastic scattering and absorption dynamics of NLMC are working properly, the reflection and transmission coefficients obtained with the NLMC simulation are compared to previously obtained analytical results and previous Monte Carlo simulations for an index matched sample.[4,32] The sample considered was 0.2 mm thick with a scattering coefficient of $\mu_s = 9.0$ mm^{-1}, anisotropy factor of $g = 0.75$, and an absorption coefficient of $\mu_a = 1.0$ mm^{-1}. A total of 25 pulses, each containing 10^6 photon packets, were averaged together to produce the results shown in Table 1.

Table 1. Comparison of an Index Matched Sample Containing Elastic Scattering and Absorption with Previous Analytical Solutions and Monte Carlo Simulations[4,32,33,a]

source	reflection	transmission
van de Hulst, 1980	0.09739	0.66096
NLMC	0.09734 ± 0.00023	0.66104 ± 0.00028
Wang et al., 1995	0.09734 ± 0.00035	0.66096 ± 0.00020
Doronin et al., 2011	0.09741 ± 0.00027	0.66096 ± 0.00017

[a]The uncertainty given represents the standard deviation.

To validate the treatment of index mismatched boundaries, an index mismatched semi-infinite slab was chosen as a second example. The slab was given an index of refraction of $n = 1.5$ compared to the background index of $n_0 = 1.0$. Scattering was assumed isotropic ($g = 0$) and a scattering coefficient of $\mu_s = 9.0$ and absorption coefficient of $\mu_a = 1.0$ were used. The excellent agreement with previous results are shown in Table 2. These results were averaged over 25 pulses each containing 10^6 photons.

Table 2. Comparison of an Index Mismatched Sample Containing Elastic Scattering and Absorption with Previous Analytical Solutions and Monte Carlo Simulations[4,34,33,a]

source	reflection
Giovanelli, 1955	0.2600
NLMC	0.25993 ± 0.00029
Wang et al., 1995	0.25907 ± 0.00170
Doronin et al., 2011	0.25957 ± 0.00043

[a]The uncertainty given represents the standard deviation.

To validate the NLMC model for SRS, we will compare the simulation results to previous experimental work on random Raman lasing in barium sulfate ($BaSO_4$) powder.[15] These results illustrated in Figure 1 demonstrate the excellent agreement between the NLMC model and experimental results. The sample used in the simulation was 5 mm deep with an index of refraction, $n = 1.6$, an anisotropy factor, $g = 0.6$, a scattering coefficient, $\mu_s = 200$ mm^{-1}, an absorption coefficient, $\mu_a = 0.1$ mm^{-1}, a spontaneous Raman coefficient, $\beta_R = 5 \times 10^{-4}$ mm^{-1}, and a stimulated Raman coefficient, $\beta_{SRS} = 1.5 \times 10^{-5}$ mm^2. The global time step was set to $\Delta t = 0.1$ ps and the bin size was set to $d = 0.02$ mm. A single incident pump pulse with a full-width at half-maximum pulse width of 50 ps and a $1/e^2$ beam diameter of 1 mm was sent into the sample, and the Raman weight exiting the sample in the reflection geometry was totaled. To generate the different pump energies, the number of pump photon packets simulated was varied over a range from 10^4 to 2×10^5. For each pump energy, 20 independent runs were computed.

Density of Raman Scattering Centers. In addition to exploring the efficiency of random Raman lasing, using the

dx.doi.org/10.1021/ph5003522 | ACS Photonics 2014, 1, 1322−1329

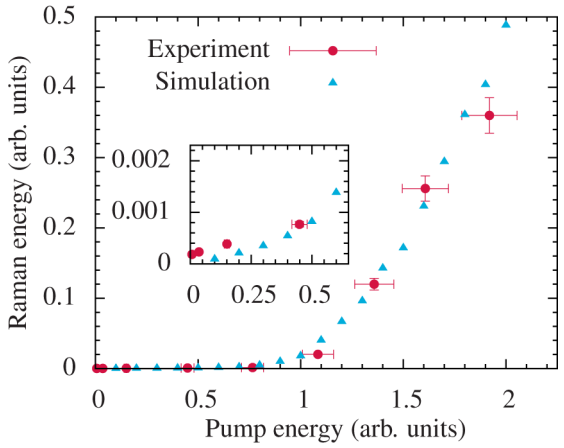

Figure 1. NLMC simulations compared with experimentally measured threshold data for random Raman lasing.[15] The error bars shown represent the 7% uncertainty in the measurements of the energy meter used and the results are the average of 20.

NLMC simulation, we can look at the distribution Raman scattering centers in the medium. The distribution of Raman scattering centers is something that can provide insight into random Raman lasing but cannot be experimentally measured. Figure 2 shows the distribution of locations where a Raman

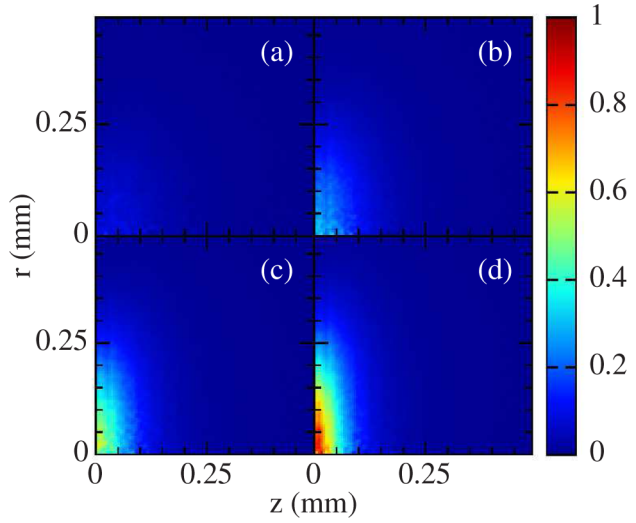

Figure 2. Density of Raman scattering centers for (a) 110000, (b) 140000, (c) 170000, and (d) 200000 incident pump photons. Intensities were normalized by the number of pump photons.

photon is converted from a pump photon, known as a Raman scattering center. The parameters used were the same as above. Each graph is normalized by the number of pump photons. What is observed here is that the vast majority of Raman photons are generated in a relatively thin region of the sample, and are not the result of long path length photons. This supports the conclusion that the majority of the random Raman lasing signal is generated near the surface of the sample where pump intensity is largest. This is in contrast to a more steady state picture where longer photon paths would experience more gain. In this transient regime picture the NLMC simulations suggest that as these long path length photons continue to travel through the medium disorder induced pump depletion occurs, leading to a lower gain at later times.[35] The net result of this process is that photons trajectories, which are present where pump intensities are greatest, are the ones most likely to contribute to random Raman lasing, and these photons need not be the ones with very long trajectories.

Scattering and Absorption Dependence. One of the most difficult properties to measure with random Raman lasing is its dependence on scattering. To date, random Raman lasing has only been observed in fibers and powders, and neither of these systems offer the chance to experimentally vary the scattering and absorption properties of the medium. Some variation of the scattering coefficient would be possible in powders by pressing the sample with a known pressure, but at some point, the particles will begin to make optical contact and will stop behaving like individual particles and will behave more like agglomerate particles.

While the dependence of SRS on scattering and absorption is difficult to experimentally realize, it is ideally suited for investigation with Monte Carlo simulations. The results are shown in Figure 3. All the parameters for these runs are the

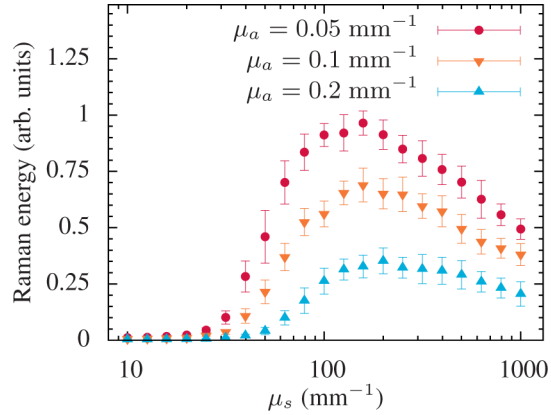

Figure 3. Dependence of SRS generation on scattering and absorption for a fixed pump intensity.

same as those used above except for the scattering and absorption coefficients. The pump energy was set to 200000 photons to correspond to the largest value used in the comparison with experiment. A clear threshold for the scattering coefficient can be seen, and this value depends on the absorption coefficient. Both, the threshold and the decrease in the random Raman emission at higher scattering coefficient can be understood by the fact that scattering is both providing feedback as well as determining the excitation volume. At low scattering, there is insufficient feedback to support gain. When scattering becomes large there is sufficient feedback, but a smaller volume of the sample is excited because the pump tends to be localized near the surface of the sample. The smaller excitation volume decreases the efficiency of the process resulting in a decrease in signal for higher scattering. These conclusions are further supported by the large decrease in the signal due to absorption near the optimum scattering coefficient. Absorption limits the size of the excitation volume, shifting the most efficient scattering coefficient toward higher scattering, and decreasing the total emission, even for the rather small absorption coefficients used here.

DISCUSSION

The probabilities used to describe the various Raman effects in the NLMC simulation can be derived from the one-dimen-

dx.doi.org/10.1021/ph5003522 | ACS Photonics 2014, 1, 1322−1329

sional equations governing the evolution of the intensity. Take for example the simplest case of spontaneous Raman scattering. In one-dimension, the intensity of Raman photons can be described by

$$\frac{dI_R}{dz} = \mu_R I_p \tag{30}$$

In between scattering events, a photon packet will travel in a straight line, thus, eq 30 describes the dynamics of a photon packet where we take the z-axis to be the direction of propagation for that photon packet. We can integrate eq 30 over the distance that it travels in its current step

$$\Delta I_R = \int_{z_0}^{z_0+(\Delta s/\mu_s)} \mu_R I_p dz \tag{31}$$

Under the assumption that this step size is small (not larger than $(c/n)\Delta t$), we can assume that the pump intensity remains constant over this small distance, thus

$$\Delta I_R \approx \mu_R(\Delta s/\mu_s) I_p \tag{32}$$

These intensities can be put in terms of photon densities using the relation $I_i = \eta\hbar c(\omega_i/n_i)\rho_i$, where i represents pump, p, or Raman, R, signals, respectively, and η is the number of photons represented per photon packet. With this, eq 32 can be rewritten in terms of the photon densities,

$$\Delta\rho_R = \mu_R(\omega_p/\omega_R)(n_R/n_p)(\Delta s/\mu_s)\rho_p \tag{33}$$

This equation has the physical interpretation that $\mu_R(\omega_p/\omega_R)(n_R/n_p)(\Delta s/\mu_s)$ is the probability that a pump photon is converted to a Raman photon. To improve the behavior of this probability, we can make use of the fact that this is small to write

$$\Delta\rho_R = (1 - e^{-\mu_R(\omega_p/\omega_R)(n_R/n_p)(\Delta s/\mu_s)})\rho_p \tag{34}$$

Now, if we write

$$\beta_R = \mu_R(\omega_p/\omega_R)(n_R/n_p) \tag{35}$$

the probability that a pump photon packet will convert to a Raman photon packet in a given step will be given by

$$P_R = 1 - e^{-\beta_R(\Delta s/\mu_s)} \tag{36}$$

which is identical to eq 26.

The same method can be used to describe the more complicated nonlinear effects of SRS. In one-dimension, the Raman signal due to SRS is described by[36,37]

$$\frac{dI_R}{dz} = GI_pI_R \tag{37}$$

where G is the Raman gain coefficient given by[38,39]

$$G = \frac{c\Delta N}{\hbar\pi^2 n_R^2 \omega_R^2 \omega_p \delta\omega_R}\frac{\partial\sigma}{\partial\Omega} \tag{38}$$

Here, ΔN is the population density (containing any thermal distributions of states) of the molecular species leading to the gain, n_R is the index of refraction at the Stokes frequency, ω_R is the Stokes frequency, ω_p is the pump frequency, $\delta\omega_R$ is the Raman line width, and $\partial\sigma/\partial\Omega$ is the Raman cross-section. Following the same procedure used for spontaneous Raman, we end up with

$$\Delta\rho_R = (1 - e^{-G\eta\hbar c(\omega_p/n_p)\rho_R(\Delta_s/\mu_s)})\rho_p \tag{39}$$

Comparing this with eq 29, we can see that our SRS coefficient relates to the Raman gain by

$$\beta_{SRS} = G\eta\hbar c(\omega_p/n_p) \tag{40}$$

Monte Carlo simulations are notorious for being computationally demanding because large numbers of photon packets must be simulated to obtain accurate dynamics. In a traditional Monte Carlo scheme such as MCML, these photon packets can travel independently indefinitely. What we mean by this is that each photon packet does not require any knowledge about any other photon packets in the simulation. This makes Monte Carlo simulations trivially parallelizable and ideal for the massive computational power of modern day GPUs.[40,41]

In NLMC, this is no longer the case. Due to nonlinear interactions, the photon packets require information about the distribution of other photon packets. This requires all parallel threads to stop, calculate the photon densities, and synchronize information. This reduces the level of parallelism; however, the NLMC code still receives an enormous speed enhancement when run on GPUs. On our system, the GPU version of the code was able to run simulations consisting of 10^6 photon packets in just a few minutes. This run time is comparable to simulations using the CPU version of the code with only 10^4 photon packets. These simulations were run using double precision accuracy on a system that consisted of an 3.4 GHz quad core CPU (Intel; i7−2600K) with 16 GB of RAM and a GPU (NVIDIA; GeForce GTX 560 Ti).

At the heart of the NLMC model is the calculation of time-resolved photon densities. The method we implemented to accomplish this is a bin sorting method. Each photon packet is sorted into bins and their weight is summed giving a measure of the photon density. This is readily parallelizable and fast; however, because a large grid must be stored, it requires a large amount of memory. On our system, GPU memory is the limiting factor to the number of photons that we can run in a single simulation. The NLMC method could be programmed in a way that this is not the case; however, there would likely be a substantial degradation in performance due to the relatively slow speed at which memory is transferred to the GPU.

In condensed matter, the Raman coefficient is typically on the order of 10^{-7} mm^{-1}.[36] With our current implementation, we are limited to a few million photon packets per pulse. With an increase in GPU memory and further optimization, it is reasonable to expect that tens of millions of photons would be possible in a reasonable amount of time. However, this is still barely approaching the level where only a few photon packets undergo spontaneous Raman scattering. Because of this computational limitation, previous Raman Monte Carlo simulations have simply taken β_R to be artificially large.[31,42] This is justified by the fact that when only spontaneous Raman effects are present β_R simply contributes a multiplicative factor on the amount of Raman generated (provided pump-depletion does not become a problem). This breaks down in the presence of SRS. When SRS effects are present, the value of both β_R and β_{SRS} play a role in the dynamics of the simulation. This can be seen in Figure 4. In practice, this does not appear to be as large of a problem as one would suspect. Figure 1 serves as an example of the accuracy of the method even with an unphysically large β_R.

dx.doi.org/10.1021/ph5003522 | ACS Photonics 2014, 1, 1322−1329

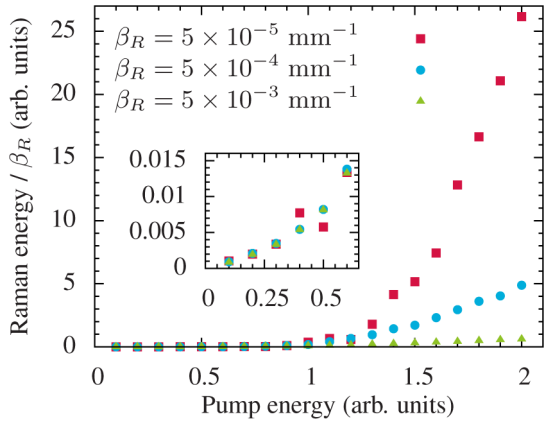

Figure 4. SRS generation with various spontaneous Raman coefficients showing that in the limit of no SRS this trivially results in a constant multiplicative factor, but in the high intensity regime, the dynamics are far more complicated.

While not explicitly included in the derivation of the probabilities used in the NLMC simulations, pump depletion is taken into account in the simulation itself. The process of converting pump photon packets into Raman photon packets removes energy from the pump field, reducing the probability of later photons converting. Thus, the mechanics of the simulation process itself take care of pump depletion effects. It should be noted, in any single global time, step pump depletion effects are ignored because the photon densities are not updated during this time. Thus, care should be taken not to use a large time step when the simulation is in the strong saturation regime.

In the NLMC simulations, there are two parameters that control the accuracy of the simulations when nonlinear effects are present, the global time step, Δt, and the photon density bin size, d. In practice, these two should be matched such that during a global time step the motion of a single photon packet does not substantially change the photon densities needed to calculate the nonlinear probabilities. To ensure this is the case, we simply require $(c/n)\Delta t \leq d$, where in this case n is taken to be the smallest index of refraction of all the layers.

To generate the random numbers for our implementation, a Hybrid Tausworthe generator was used.[43] This generator has the advantage of being faster and requiring less memory than a Mersenne twister method,[44] while still providing a period greater than 10^{36}. To generate these numbers in parallel each photon packet is assigned its own set of four initial seeds generated using the built-in random number generator, which is itself seeded with the current time, ensuring each run is independent of the last.

In the current NLMC code, only SRS is considered; however, the concept of introducing intensity dependent coefficients by way of computing the photon density is not limited to just these effects. This idea can be generalized in a straightforward manner to handle other nonlinear effects like absorption saturation, second and third harmonic generation, coherent anti-Stokes Raman scattering (CARS), and so on. Additionally, higher order Stokes and anti-Stokes processes can be treated by allowing Stokes photons to undergo additional Stokes processes.[45]

In the treatment here, we have assumed that each wavelength propagates through the simulation using the same optical properties. Wavelength-dependent properties could easily be implemented by defining a new set of optical properties for each type of photon and keeping track of this throughout the simulation.

It is important to note that, while this technique shows excellent agreement with experimental data, it neglects the wave nature of light. All phase matching conditions are automatically satisfied for SRS. Thus, it is not a coherent wave mixing phenomena, but is more closely related to stimulated emission, where the newly created photon's phase depends only on the phase of the stimulating photon and not on the phase of the pump photon. However, the generated intensity does not depend on the phase of the stimulating photon. In other words, the process has the same probability of occurring, regardless of this phase.

Currently, there are no methods capable of accounting for the wave effects of light propagation in turbid media in the presence of nonlinear optical effects. However, for very simple systems, finite difference time domain (FDTD)[46] methods might be possible, but this approach is ultimately limited by the requirement that the location of each scattering particle must be known. Additionally, extending the probabilistic approach of describing SRS employed here to electric field Monte Carlo (EMC) simulations[47−49] exists, but such methods still treat light as local particles with definite direction instead of waves that do not have a well-defined direction.

Here we have presented a method for including nonlinear effects into Monte Carlo simulations, specifically SRS. The ability to include these effects in Monte Carlo simulations will allow for a better understanding of the nonlinear dynamics of light in a turbid media, advancing fields such as nonlinear microscopy of biological tissues and increasing our understanding of new fundamental effects, such as random Raman lasing.

AUTHOR INFORMATION

Corresponding Author

*E-mail: brett.hokr@tamu.edu.

Notes

The authors declare no competing financial interest.

ACKNOWLEDGMENTS

The authors would like to thank George W. Kattawar for helpful discussions. This work was partially supported by National Science Foundation Grants ECCS-1250360, DBI-1250361, CBET-1250363, PHY-1241032 (INSPIRE CREATIV), PHY-1068554, EEC-0540832 (MIRTHE ERC), and the Robert A. Welch Foundation (Award A-1261).

REFERENCES

(1) Plass, G. N.; Kattawar, G. W. Monte Carlo calculations of light scattering from clouds. *Appl. Opt.* **1968**, *7*, 415−419.

(2) Wilson, B. C.; Adam, G. A Monte Carlo model for the absorption and flux distributions of light in tissue. *Med. Phys.* **1983**, *10*, 824−830.

(3) Keijzer, M.; Jacques, S. L.; Prahl, S. A.; Welch, A. J. Light distributions in artery tissue: Monte Carlo simulations for finite-diameter laser beams. *Lasers Surg. Med.* **1989**, *9*, 148−154.

(4) Wang, L.; Jacques, S. L.; Zheng, L. MCML - Monte Carlo modeling of light transport in multi-layered tissues. *Comput. Meth. Prog. Bio.* **1995**, *47*, 131−146.

(5) Kirk, D. B.; Hwu, W.-m. W. *Programming Massively Parallel Processors: A Hands-on Approach*, 2nd ed.; Elsevier: Waltham, MA, 2012; p 514.

(6) Hendricks, J. S.; Booth, T. E. In *Monte-Carlo Methods Appl. Neutronics, Photonics Stat. Phys.*; Alcouffe, R., Dautray, R., Forster, A.,

Ledanois, G., Mercier, B., Eds.; Lecture Notes in Physics; Springer: Berlin Heidelberg, 1985; Vol. *240*, pp 83−92.
(7) Qu, J. Y.; MacAulay, C. E.; Lam, S.; Palcic, B. Laser-induced fluorescence spectroscopy at endoscopy: tissue optics, Monte Carlo modeling, and in vivo measurements. *Opt. Eng.* **1995**, *34*, 3334−3343.
(8) Welch, A. J.; Gardner, C.; Richards-Kortum, R.; Chan, E.; Criswell, G.; Pfefer, J.; Warren, S. Propagation of fluorescent light. *Lasers Surg. Med.* **1997**, *21*, 166−178.
(9) Liu, Q.; Zhu, C.; Ramanujam, N. Experimental validation of Monte Carlo modeling of fluorescence in tissues in the UV-visible spectrum. *J. Biomed. Opt.* **2003**, *8*, 223−236.
(10) Churmakov, D. Y.; Meglinski, I. V.; Greenhalgh, D. A. Amending of fluorescence sensor signal localization in human skin by matching of the refractive index. *J. Biomed. Opt.* **2004**, *9*, 339−346.
(11) Enejder, A. M. K.; Koo, T.-W.; Oh, J.; Hunter, M.; Sasic, S.; Feld, M. S.; Horowitz, G. L. Blood analysis by Raman spectroscopy. *Opt. Lett.* **2002**, *27*, 2004−2006.
(12) Matousek, P.; Morris, M. D.; Everall, N.; Clark, I. P.; Towrie, M.; Draper, E.; Goodship, A.; Parker, A. W. Numerical simulations of subsurface probing in diffusely scattering media using spatially offset Raman spectroscopy. *Appl. Spectrosc.* **2005**, *59*, 1485−1492.
(13) Keller, M. D.; Wilson, R. H.; Mycek, M.-A.; Mahadevan-Jansen, A. Monte Carlo model of spatially offset Raman spectroscopy for breast tumor margin analysis. *Appl. Spectrosc.* **2010**, *64*, 607−614.
(14) Hokr, B. H.; Yakovlev, V. V. Raman signal enhancement via elastic light scattering. *Opt. Express* **2013**, *21*, 11757−11762.
(15) Hokr, B. H.; Bixler, J. N.; Cone, M.; Mason, J. D.; Beier, H. T.; Noojin, G. D.; Petrov, G. I.; Golovan, L. A.; Thomas, R. J.; Rockwell, B. A.; Yakovlev, V. V. Bright emission from a random Raman laser. *Nat. Commun.* **2014**, *5*, 4356.
(16) Hokr, B. H.; Bixler, J. N.; Noojin, G. D.; Thomas, R. J.; Rockwell, B. A.; Yakovlev, V. V.; Scully, M. O. Single-shot stand-off chemical identification of powders using random Raman lasing. *Proc. Natl. Acad. Sci. U.S.A.* **2014**, *111*, 12320−12324.
(17) Chaigne, T.; Katz, O.; Boccara, A. C.; Fink, M.; Bossy, E.; Gigan, S. Controlling light in scattering media non-invasively using the photoacoustic transmission matrix. *Nat. Photonics* **2014**, *8*, 58−64.
(18) Bertolotti, J.; van Putten, E. G.; Blum, C.; Lagendijk, A.; Vos Willem, L.; Mosk, A. P. Non-invasive imaging through opaque scattering layers. *Nature* **2012**, *491*, 232−234.
(19) Evans, C. L.; Potma, E. O.; Puoris'haag, M.; Côté, D.; Lin, C. P.; Xie, X. S. Chemical Imaging of tissue in vivo with video-rate coherent anti-Stokes Raman scattering microscopy. *Proc. Natl. Acad. Sci. U.S.A.* **2005**, *102*, 16807−16812.
(20) Kee, T. W.; Cicerone, M. T. Simple approach to one-laser, broadband coherent anti-Stokes Raman scattering microscopy. *Opt. Lett.* **2004**, *29*, 2701−2703.
(21) Petrov, G. I.; Arora, R.; Yakovlev, V. V.; Wang, X.; Sokolov, A. V.; Scully, M. O. Comparison of coherent and spontaneous Raman microspectroscopies for noninvasive detection of single bacterial endospores. *Proc. Natl. Acad. Sci. U.S.A.* **2007**, *104*, 7776−7779.
(22) Arora, R.; Petrov, G. I.; Yakovlev, V. V.; Scully, M. O. Detecting anthrax in the mail via coherent Raman microspectroscopy. *Proc. Natl. Acad. Sci. U.S.A.* **2012**, *109*, 1151−1153.
(23) Horton, N. G.; Wang, K.; Kobat, D.; Clark, C. G.; Wise, F. W.; Schaffer, C. B.; Xu, C. In vivo three-photon microscopy of subcortical structures within an intact mouse brain. *Nat. Photonics* **2013**, *7*, 205−209.
(24) Arora, R.; Petrov, G. I.; Yakovlev, V. V.; Scully, M. O. Chemical analysis of molecular species through turbid medium. *Anal. Chem.* **2014**, *86*, 1445−1451.
(25) Blanca, C. M.; Saloma, C. Monte Carlo analysis of two-photon fluorescence imaging through a scattering medium. *Appl. Opt.* **1998**, *37*, 8092−8102.
(26) Deng, X.; Gu, M. Penetration depth of single-, two-, and three-photon fluorescence microscopic imaging through human cortex structures: Monte Carlo simulation. *Appl. Opt.* **2003**, *42*, 3321−3329.
(27) Leray, A.; Odin, C.; Huguet, E.; Amblard, F.; Le Grand, Y. Spatially distributed two-photon excitation fluorescence in scattering media: experiments and time-resolved Monte Carlo simulations. *Opt. Commun.* **2007**, *272*, 269−278.
(28) Box, G. E. P.; Muller, M. E. A note on the generation of random normal deviates. *Ann. Math. Stat.* **1958**, *29*, 610−611.
(29) Burden, R. L.; Faires, J. D. *Numerical Analysis*, 9th ed.; Brookes/Cole: Boston, MA, 2010; p 861.
(30) Brent, R. P. *Algorithms for Minimization Without Derivatives*, 1st ed.; Dover Publications: Mineola, New York, 1973; p 195.
(31) Everall, N.; Hahn, T.; Matousek, P.; Parker, A. W.; Towrie, M. Photon migration in Raman spectroscopy. *Appl. Spectrosc.* **2004**, *58*, 591−597.
(32) de Hulst, H. C. *Multiple Light Scattering: Tables, Formulas, and Applications*; Academic Press: New York, 1980.
(33) Doronin, A.; Meglinski, I. Online object oriented Monte Carlo computational tool for the needs of biomedical optics. *Biomed. Opt. Express* **2011**, *2*, 2461−2469.
(34) Giovanelli, R. G. Reflection by semi-infinite diffusers. *Opt. Acta* **1955**, *2*, 153−162.
(35) Bachelard, N.; Gaikwad, P.; Backov, R.; Sebbah, P.; Vallée, R. A. L. Disorder as a Playground for the Coexistence of Optical Nonlinear Effects: Competition between Random Lasing and Stimulated Raman Scattering in Complex Porous Materials. *ACS Photonics* **2014**, DOI: 10.1021/ph500280m.
(36) Boyd, R. W. *Nonlinear Opt.*, 2nd ed.; Academic Press: New York, 2003.
(37) Bloembergen, N. The stimulated Raman effect. *Am. J. Phys.* **1967**, *35*, 989−1023.
(38) Martin, W. E.; Winfield, R. J. Nonlinear effects on pulsed laser propagation in the atmosphere. *Appl. Opt.* **1988**, *27*, 567−577.
(39) Hokr, B. H.; Noojin, G. D.; Petrov, G. I.; Beier, H. T.; Thomas, R. J.; Rockwell, B. A.; Yakovlev, V. V. How to drive CARS in reverse. *J. Mod. Opt.* **2014**, *61*, 53−56.
(40) Fang, Q.; Boas, D. A. Monte Carlo simulation of photon migration in 3D turbid media accelerated by graphics processing units. *Opt. Express* **2009**, *17*, 20178.
(41) Doronin, A.; Meglinski, I. Peer-to-peer Monte Carlo simulation of photon migration in topical applications of biomedical optics. *J. Biomed. Opt.* **2012**, *17*, 90504.
(42) Hokr, B. H.; Yakovlev, V. V. A proposal for a random Raman laser. *J. Mod. Opt.* **2014**, *61*, 57−60.
(43) Nguyen, H. *GPU Gems 3*, 1st ed.; Addison-Wesley Professional: Boston, MA, 2007.
(44) Matsumoto, M.; Nishimura, T. Mersenne twister: a 623-dimensionally equidistributed uniform pseudo-random number generator. *ACM Trans. Model. Comput. Simul.* **1998**, *8*, 3−30.
(45) Hokr, B. H.; Bixler, J. N.; Yakovlev, V. V. Higher order processes in random Raman lasing. *Appl. Phys. A: Mater. Sci. Process.* **2014**, *117*, 681−685.
(46) Taflove, A.; Hagness, S. C. *Computational Electrodynamics: The Finite-Difference Time-Domain Method*, 3rd ed.; Artech House: Norwood, MA, 2005.
(47) Xu, M. Electric field Monte Carlo simulation of polarized light propagation in turbid media. *Opt. Express* **2004**, *12*, 6530.
(48) Doronin, A.; Macdonald, C.; Meglinski, I. Propagation of coherent polarized light in turbid highly scattering medium. *J. Biomed. Opt.* **2014**, *19*, 025005.
(49) Doronin, A.; Radosevich, A. J.; Backman, V.; Meglinski, I. Two electric field Monte Carlo models of coherent backscattering of polarized light. *J. Opt. Soc. Am. A* **2014**, *31*, 2394.